ACS Energy LETTERS

http://pubs.acs.org/journal/aelccp

Efficient Wide-Bandgap Mixed-Cation and Mixed-Halide Perovskite Solar Cells by Vacuum Deposition

Lidón Gil-Escrig, Chris Dreessen, Francisco Palazon, Zafer Hawash, Ellen Moons, Steve Albrecht, Michele Sessolo,* and Henk J. Bolink

Cite This: *ACS Energy Lett.* 2021, 6, 827−836

Read Online

ACCESS | Metrics & More | Article Recommendations | Supporting Information

ABSTRACT: **Vacuum deposition methods are increasingly applied to the preparation of perovskite films and devices, in view of the possibility to prepare multilayer structures at low temperature. Vacuum-deposited, wide-bandgap solar cells based on mixed-cation and mixed-anion perovskites have been scarcely reported, due to the challenges associated with the multiple-source processing of perovskite thin films. In this work, we describe a four-source vacuum deposition process to prepare wide-bandgap perovskites of the type $FA_{1-n}Cs_nPb(I_{1-x}Br_x)_3$ with a tunable bandgap and controlled morphology, using FAI, CsI, PbI_2, and $PbBr_2$ as the precursors. The simultaneous sublimation of PbI_2 and $PbBr_2$ allows the relative Br/Cs content to be decoupled and controlled, resulting in homogeneous perovskite films with a bandgap in the 1.7−1.8 eV range and no detectable halide segregation. Solar cells based on 1.75 eV bandgap perovskites show efficiency up to 16.8% and promising stability, maintaining 90% of the initial efficiency after 2 weeks of operation.**

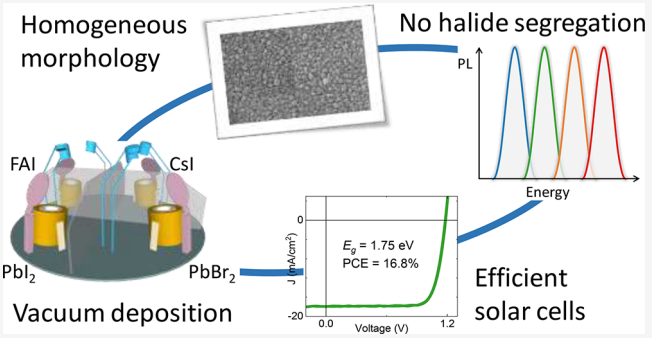

Among emerging photovoltaic (PV) technologies, thin-film solar cells based on organic−inorganic (hybrid) lead halide perovskites (herein called perovskites) are by far the most widely investigated. The interest toward these materials is driven by the possibility to deposit high-quality semiconducting films with simple and low-energy-demanding processes.[1−6] This feature is a consequence of the high tolerance to defects,[7,8] conferring perovskites with low trap density and long carrier diffusion length.[9−14] As a result, the efficiency of single-junction solar cells has grown considerably within only a decade of development,[15] with a record power conversion efficiency (PCE) now exceeding 25%.[16] An important property of perovskites is the possibility to readily tune their bandgap,[17−20] making them a suitable candidate for applications in single-junction as well as multijunction solar cells,[21−24] e.g., in combination with narrow-bandgap absorbers such as $Cu(In,Ga)Se_2$[25−28] and silicon[29−35] or by using complementary perovskites.[36−42] Perovskite alloys of the type $ASn_{1-x}Pb_xI_3$ (where A is an organic or inorganic cation or a mixture of them) have bandgaps in the 1.20−1.25 eV range for lead content $0.25 \leq x \leq 0.5$.[43,44] This requires perovskite compositions with wide bandgaps in the 1.75−1.85 eV range in order to aim at perovskite−perovskite tandem devices that can exceed the theoretical efficiency limit of single-junction solar cells.[21−24] Perovskite films with wide bandgaps suitable for perovskite−perovskite tandems can be readily obtained by using mixed-iodide/bromide formulations,[17] and mixed-A-site cations are also employed to improve the photo- and thermal stability of the compounds.[45−47] The study of wide-bandgap perovskite materials and solar cells is a booming field of research, well summarized in recent reviews[23,48] and in research articles containing some of the best performing devices to date.[49−51] In comparison with narrower-bandgap materials,[52] wide-bandgap perovskite solar cells suffer from a larger open-circuit voltage (V_{oc}) deficit, i.e., the V_{oc} does not scale linearly with the bandgap as predicted by the Shockley−Queisser (SQ) limit. This deviation is due to nonradiative recombination in the perovskite bulk and at the interface with the transport layers.[51,53−55] For this reason, a large number of studies aimed at developing bulk and surface passivation

Received: November 23, 2020
Accepted: January 28, 2021
Published: February 3, 2021

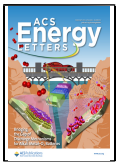

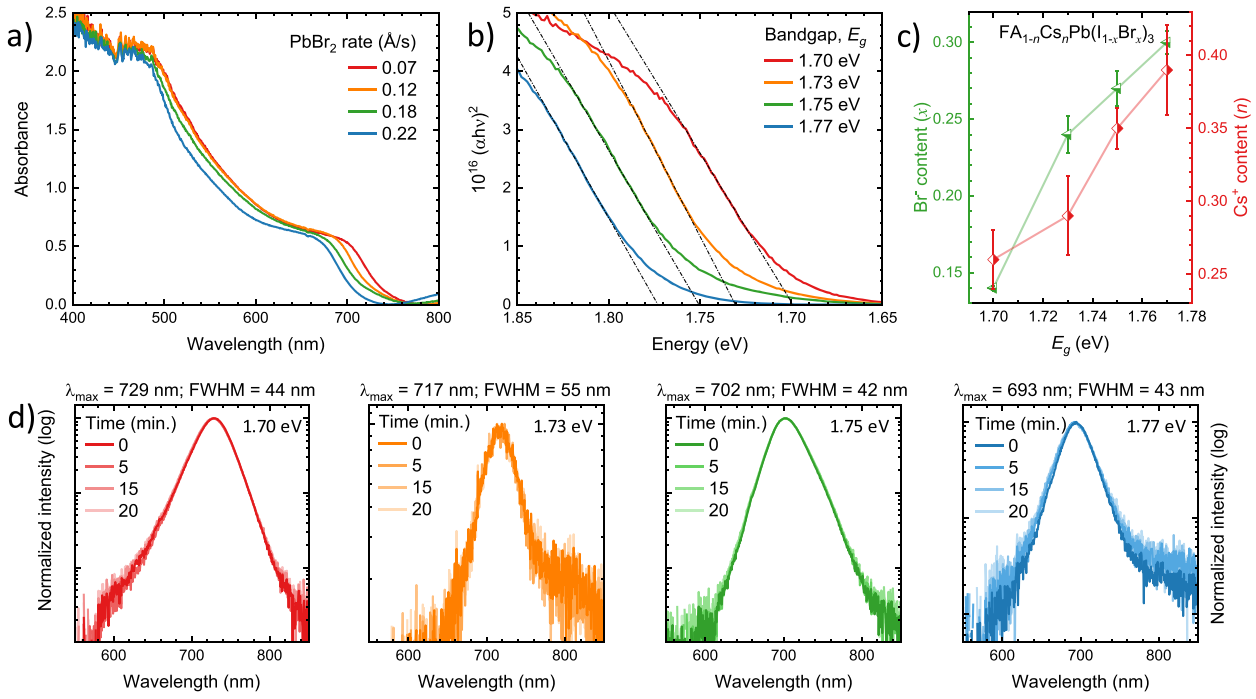

Figure 1. (a) Absorbance spectra of a series of $FA_{1-n}Cs_nPb(I_{1-x}Br_x)_3$ perovskite films obtained with increasing $PbBr_2$ deposition rate and (b) corresponding Tauc plot and estimated bandgap energies (E_g). The film thickness is 500 nm for all samples. (c) Bulk bromide (left, green) and cesium (right, red) content in the perovskite films estimated by energy dispersive X-ray spectroscopy (EDS). Error bars are the standard deviation of measurements obtained from films of different deposition runs. (d) Normalized photoluminescence (PL) spectra of the same samples recorded over time (up to 20 min) under continuous illumination. The excitation source is a green laser (515 nm) with an irradiance of approximately 300 mW/cm^2.

strategies as well as identifying suitable transport layers and contacts.[56−60]

The vast majority of studies on wide-bandgap perovskite solar cells relied on solution-processed perovskite thin films. Vacuum deposition is an alternative method with superior control over the film thickness and composition; it is compatible with large areas and eliminates the processing concerns related with the use of solvents.[61−63] This is especially relevant for the fabrication of complex multilayer architectures, necessary for tandem solar cells.[37,64] Moreover, vacuum deposition allows the deposition of pinhole-free, uniform, and smooth films.[65−68] Early reports on vacuum-deposited wide-bandgap perovskites used the simplest formulation, methylammonium lead iodide−bromide, $MAPb(I_{1-x}Br_x)_3$. We showed that this type of compound with a bandgap (E_g) up to 1.7 eV ($x \approx 0.2$) is stable even at high irradiance levels, and the corresponding perovskite solar cells exhibited a PCE up to 15.9%.[69] When the amount of bromide is increased ($x \geq 0.3$), the perovskite demixes into iodide- and bromide-rich phases in a process known as "halide segregation",[45,70,71] which can be readily monitored from the red-shifted perovskite photoluminescence (PL) spectrum.[69,72] The iodide-rich, narrow-bandgap regions can reduce the quasi-Fermi level splitting (QFLS) and hence the maximum attainable V_{oc}. Phase-stable hybrid perovskite films with E_g > 1.7 eV require the use of mixed-A-site cations such as cesium and formamidinium (Cs^+, FA^+).[45−47] We have previously demonstrated the deposition of the wide-bandgap $Cs_{0.5}FA_{0.4}MA_{0.1}Pb(I_{0.83}Br_{0.17})_3$ perovskite in a four-source cosublimation process, from PbI_2, CsBr, formamidinium iodide (FAI), and methylammonium iodide (MAI) precursors.[73] CsBr was used simultaneously as the source of Cs^+ and Br^-, a strategy later adopted by others to reduce the number of deposition sources and precursors.[74,75] In those recent reports, $FA_{1-n}Cs_nPb(I_{1-x}Br_x)_3$ perovskites with intentionally low CsBr content ($x \leq 0.1$) were presented, targeting perovskites with bandgaps more suitable for single-junction solar cells. In order to obtain a wide bandgap (E_g > 1.7 eV), a substantial amount of Br^- needs to be incorporated, hence resulting in an equally large cesium concentration. The excess of cesium was found to cause an irregular morphology and substantial bulk recombination in the perovskite, limiting the device performance.[73]

In this work, we demonstrate an alternative four-source vacuum deposition process to prepare wide-bandgap perovskites of the type $FA_{1-n}Cs_nPb(I_{1-x}Br_x)_3$ with a tunable bandgap and controlled morphology, using FAI, CsI, PbI_2, and $PbBr_2$ as the precursors. The simultaneous sublimation of the two lead halides allows the relative bromide/cesium content to be decoupled and controlled, resulting in homogeneous perovskite films with a bandgap in the 1.7−1.8 eV range and no detectable halide segregation. Solar cells based on 1.75 eV bandgap perovskites show a PCE up to 16.8% and promising stability, maintaining 90% of the initial efficiency after 2 weeks of continuous operation in inert atmosphere.

The mixed-cation lead mixed-halide perovskites were deposited by simultaneous vacuum deposition of the precursors FAI, CsI, PbI_2, and $PbBr_2$. In order to calibrate the deposition rate of each material, the specific tooling factors were determined by individually subliming them and

https://doi.org/10.1021/acsenergylett.0c02445
ACS Energy Lett. 2021, 6, 827−836

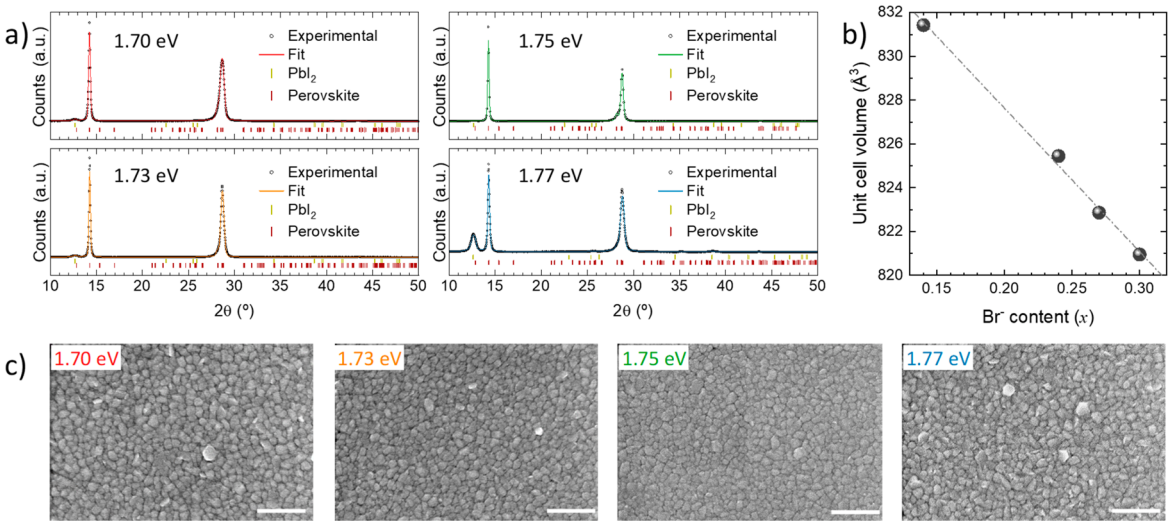

Figure 2. (a) Whole-pattern Le Bail fit (colored lines) of XRD patterns (open black circles). Vertical markers correspond to calculated Bragg's reflections for a distorted perovskite phase (dark red) and PbI_2 (yellow). (b) Calculated unit cell volumes as obtained from fit as a function of the bromide content estimated by EDS. (c) Surface morphology of the whole sample series as observed by SEM; scale bar corresponds to 500 nm.

comparing the thickness displayed from the quartz crystal microbalance (QCM) with the one measured with a mechanical profilometer. Unlike MAI, which exhibits non-standard sublimation properties,[76] the FAI adhesion is rather independent of the chemical composition of the surface,[77] and hence, the FAI deposition rate can be monitored with a dedicated QCM placed nearby the corresponding thermal source. The details of the experimental conditions are provided in the Supporting Information. We prepared four perovskite compositions with increasing Br^-/I^- and Cs^+/FA^+ ratios, with the aim to increase the bandgap while ensuring phase stability. After several variations, we found the following procedure to lead to the best performing perovskite compositions. The FAI and PbI_2 deposition rates were kept constant at 0.8 and 1 Å/s, respectively. The $PbBr_2$ deposition rate was varied from 0.07 to 0.22 Å/s, while the CsI rate was increased from 0.25 to 0.45 Å/s, to prevent halide segregation in the bromide-rich formulations. The substrates were kept at room temperature (RT) during deposition, and the films were not annealed and used as-deposited.

The absorbance spectra of a series of 500 nm thick wide-bandgap $FA_{1-n}Cs_nPb(I_{1-x}Br_x)_3$ perovskite films on glass substrates are reported in Figure 1a. All films show the expected perovskite absorption profile, with absorbance >1 for wavelengths below approximately 550 nm. With increasing $PbBr_2$ content (deposition rate), we observed the expected blue-shift of the absorption cutoff from approximately 740 to 690 nm, indicating that indeed bromide is incorporated into the perovskite structure. The corresponding Tauc plots (Figure 1b) allow the bandgap energy of the four perovskite compositions to be estimated, with E_g increasing steadily from 1.70 to 1.77 eV. The bulk Cs^+ (n) and Br^- (x) concentrations in the different $FA_{1-n}Cs_nPb(I_{1-x}Br_x)_3$ samples were estimated by energy dispersive X-ray spectroscopy (EDS). As highlighted in Figure 1c, bromide and cesium contents were found to be in the $0.14 \leq x \leq 0.30$ and $0.26 \leq n \leq 0.39$ ranges, respectively. The Cs^+ concentration was adjusted in order to stabilize the perovskite formulations against halide segregation, in particular when the bromide content is increased to obtain the wider-bandgap materials. In Figure S1, the photoluminescence (PL) spectra of perovskite films with a 1.75 eV bandgap ($x = 0.27$) and varying amounts of Cs+ (n) are presented, showing that the perovskite is photostable for CsI deposition rates >0.3 Å/s ($n > 0.3$, see discussion in the Supporting Information and Figure S2). For this particular perovskite (E_g = 1.75 eV), we have performed further compositional analysis by using high-resolution X-ray photoemission spectroscopy (HR-XPS) to measure the core levels of the perovskite elements. The collected spectra were consequently normalized, using the corresponding atomic sensitivity factors, to find the surface atomic composition.[78] The surface contents of bromide and cesium using HR-XPS were found to be $x = 0.24$ and $n = 0.40$, respectively (Figure S3), only slightly different from the values obtained by EDS. Taking the difference in information depth into consideration for XPS[79] (only a few nanometers) and EDS[80] (several hundreds of nanometers), the results imply that there is no substantial compositional difference between the bulk and the surface of the perovskite films. In Figure 1d, the PL spectra of the entire series of stabilized perovskite films is reported. Spectra are collected over time under continuous wave laser illumination (515 nm), at an irradiance of approximately 300 mW/cm^2, corresponding to a 5−6 sun of equivalent intensity. Note that after an initial drop of the PL intensity in the first 15−20 min, we found it to be stable for up to 1 h of continuous measurement (Figure S4). Even with these harsh conditions, we did not observe any low-energy PL components, which would indicate halide segregation into iodide-rich regions. Note that a semilogarithmic scale is used for all spectra in Figure 1d to highlight the persistence of a single PL component. The differences in line width are due to varying signal-to-noise ratios among the different samples, hence the full width at half-maximum (fwhm) measured by a Gaussian fit is reported for reference. We observed photo-induced halide segregation only when the bromide content x was increased to 0.4 (Figure S5), indicating that the perovskite formulation should be substantially modified in order to obtain phase-stable materials with higher bromide content. We have also measured the PL spectra for a perovskite film on glass, exciting the sample both from the glass and from the

https://doi.org/10.1021/acsenergylett.0c02445
ACS Energy Lett. 2021, 6, 827−836

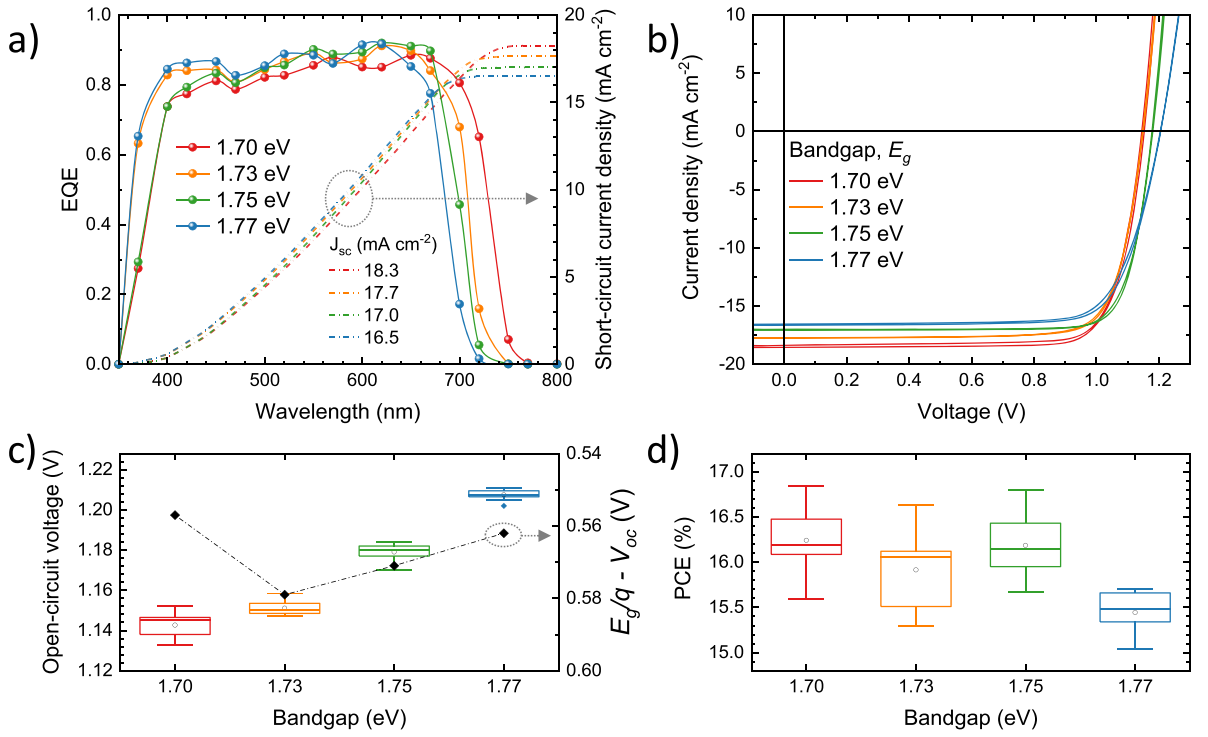

Figure 3. Characterization of wide-bandgap perovskite solar cells with $FA_{1-n}Cs_nPb(I_{1-x}Br_x)_3$ absorbers in a p−i−n configuration. (a) External quantum efficiency (EQE) spectra (line and symbols) and corresponding short-circuit current-density (J_{sc}, dotted lines) calculated by integration of each EQE spectrum with the global AM1.5G solar spectrum. (b) $J-V$ curves under simulated solar illumination recorded in forward (from short to open circuit) and reverse (from open to short circuit) bias for representative pixels. Summary of the (c) open-circuit voltage (V_{oc}) and (d) power conversion efficiency (PCE) measured for perovskite solar cells as a function of the bandgap determined from Tauc analysis. In the right axis in (c), the open-circuit voltage deficit ($E_g/q - V_{oc}$) is also reported (lines are guides to the eye).

perovskite side. As shown in Figure S6, the spectral shape and position is unaltered, suggesting that there are no obvious compositional changes through the cross section of the film. The lower PL intensity observed when shining the laser directly on the perovskite film indicates a larger degree of nonradiative recombination at the perovskite surface. In order to estimate the reproducibility of the deposition process, we compared the PL spectra for films obtained from seven consecutive deposition runs. As depicted in Figure S7, the bandgap variation for seven different batches of the perovskite with a bandgap of 1.75 eV is only 17 meV, demonstrating the good reproducibility of the vacuum deposition process.

The perovskite films were further analyzed by X-ray diffraction (XRD, Figure 2a). The XRD data can be fitted considering a single distorted perovskite phase in combination with a marginal contribution from PbI_2, which is mostly visible by its main peak around 2θ = 12.8°. The perovskite phase considered here corresponds to the space group *Pnma* (orthorhombic system), which is the reported stable phase of $CsPbBr_3$ at room temperature as well as of $MAPbBr_3$ at low temperature (see Inorganic Crystal Structure Database, ICSD references #243735 and #158306). This can be considered a lower-symmetry derivative (hettotype) of the highest-symmetry cubic perovskite (aristotype; space group *Pm*-3m), where PbX_6 octahedra are slightly tilted (see scheme in Figure S8).[81] All samples show a clear preferential orientation along the *b*-axis (perpendicular to the substrate), as evidenced by the two main reflections at 2θ = 14.2° and 2θ = 28.7°, which are ascribed to the (020) and (040) planes. The unit cell volumes derived from the whole-pattern Le Bail fits presented in Figure 2a are plotted in Figure 2b, showing a clear shrinkage of the unit cell from 831.5 to 821 Å^3 as more iodide anions are replaced by bromide anions, which have a smaller ionic radius (as well as FA^+ being replaced by Cs^+, though this replacement typically has a smaller effect in the lattice expansion or shrinkage than the anion exchange). The different values obtained by the whole-pattern fits are the result of small shifts of the XRD peaks, which can be better visualized in Figure S9.

We also studied the morphology of the $FA_{1-n}Cs_nPb(I_{1-x}Br_x)_3$ thin films by SEM top view images (Figure 2c). All films exhibit a similar surface morphology, composed of small grains (typical size in the 50−100 nm range) arranged in a compact and homogeneous manner. Such small grains are a common feature of vacuum-deposited perovskite films, as highlighted in several previous reports.[82−84] The morphology of these materials is in stark contrast with what we have observed before for vacuum-deposited $Cs_{0.5}FA_{0.4}MA_{0.1}Pb(I_{0.83}Br_{0.17})_3$ films, obtained using CsBr as a simultaneous precursor for Cs^+ and Br^-.[73] As discussed in the introduction, that process does not allow to the contents of the two ions (Cs^+ and Br^-) to be separately fine-tuned, leading to irregular morphology with randomly oriented grains growing on the perovskite surface.

To shortly summarize, we demonstrated the successful room temperature deposition of highly oriented $FA_{1-n}Cs_nPb(I_{1-x}Br_x)_3$ films with homogeneous morphology and controlled and tunable bandgap from 1.70 to 1.77 eV. This is achieved with a four-source vacuum deposition process, using FAI, CsI,

https://doi.org/10.1021/acsenergylett.0c02445
ACS Energy Lett. 2021, 6, 827−836

Table 1. Average Photovoltaic Parameters with Standard Deviation Extracted from $J-V$ Curves under Simulated Solar Illumination from Wide-Bandgap Perovskite Solar Cells with $FA_{1-n}Cs_nPb(I_{1-x}Br_x)_3$ in p−i−n Configuration[a]

composition	E_g (eV)	J_{sc} (mA cm^{-2})	FF (%)	V_{oc} (mV)	PCE (%)
$FA_{0.74}Cs_{0.26}Pb(I_{0.86}Br_{0.14})_3$	1.70	18.3 ± 0.2	77.5 ± 0.9	1142 ± 6	16.2 ± 0.3
$FA_{0.71}Cs_{0.29}Pb(I_{0.76}Br_{0.24})_3$	1.73	17.7 ± 0.1	77.5 ± 1.2	1151 ± 3	15.9 ± 0.4
$FA_{0.65}Cs_{0.35}Pb(I_{0.73}Br_{0.27})_3$	1.75	17.0 ± 0.1	80.3 ± 0.8	1179 ± 4	16.2 ± 0.3
$FA_{0.61}Cs_{0.39}Pb(I_{0.70}Br_{0.30})_3$	1.77	16.6 ± 0.1	76.1 ± 0.8	1208 ± 2	15.5 ± 0.2

[a]At least 12 cells for each bandgap have been tested.

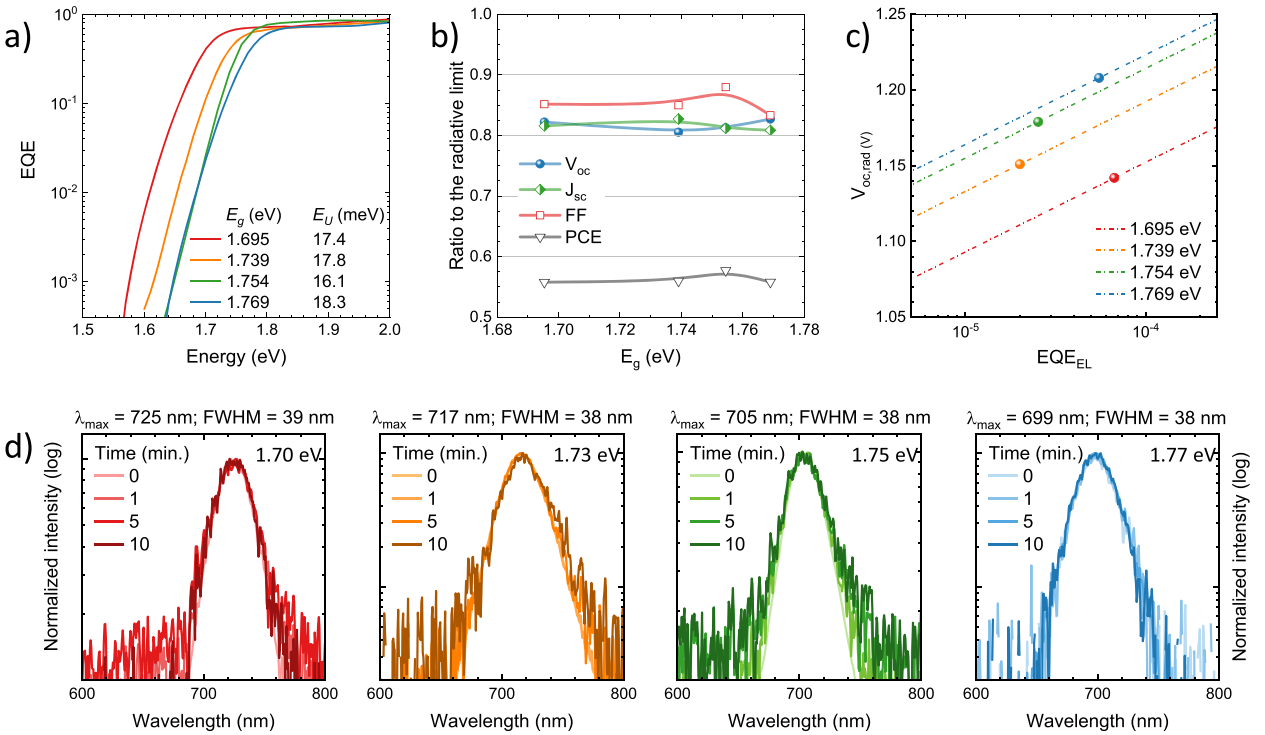

Figure 4. Optoelectronic analysis of $FA_{1-n}Cs_nPb(I_{1-x}Br_x)_3$ solar cells with different bandgaps. (a) Sensitive EQE spectra in the bandgap region and calculated bandgap and Urbach energies. (b) Ratio of measured V_{oc}, J_{sc}, and FF to their maximum theoretical (radiative) limit (lines are guides to the eye). (c) Relation between the open-circuit voltage in the radiative limit with the electroluminescence quantum efficiency, EQE_{EL}.of a solar cell (lines) for the four bandgaps studied here. Symbols shows the measured V_{oc}, allowing the corresponding EQE_{EL} to be estimated. (d) Electroluminescence (EL) spectra of the same samples recorded over time (up to 10 min) under continuous forward bias. Each cell was driven with a constant current-density equal to the J_{sc} obtained under simulated solar illumination.

PbI_2, and $PbBr_2$ as the precursors. The use of $PbBr_2$ and CsI is important to control the relative bromide/cesium content in each sample, which is found to be stable against photoinduced halide segregation. In view of the favorable properties of the perovskite films presented above, we used them as the light-absorbing layer in fully vacuum-deposited perovskite solar cells. We fabricated p−i−n solar cells with the structure reported in Figure S10. Briefly, patterned indium tin oxide (ITO) transparent electrodes were coated with MoO_3 (5 nm) to enhance hole transfer between ITO and the hole transport layer (HTL), a 10 nm thick film of *N*4,*N*4,*N*4″,*N*4″-tetra([1,1′-biphenyl]-4-yl)-[1,1′:4′,1″-terphenyl]-4,4″-diamine (TaTm, 10 nm). Afterward, a 500 nm thick perovskite film was deposited on top and capped with an electron transport layer (ETL, C_{60}, 25 nm). A thin (8 nm) film of bathocuproine (BCP) was used to ensure ohmic contact in between the ETL and a silver electrode (100 nm thick). Further details of the solar cell fabrication are reported in the Supporting Information.

The external quantum efficiency (EQE, Figure 3a) spectra were found to be similarly high (in the 0.8−0.9 range) for the four materials through the whole visible spectrum. The onset of the spectral response in the low-energy regime follows the trend expected from the perovskites' optical absorption and bandgap (Figure 1), i.e., the EQE onset shifts to lower wavelengths when the content of bromide is increased. The corresponding short-circuit currents (J_{sc}), calculated by integration of the EQE over the global AM1.5G solar spectra, decrease from 18.3 to 16.5 mA cm^{-2} when widening the bandgap from 1.70 to 1.77 eV. These values agree with those extracted from current-density vs voltage ($J-V$) curves under simulated solar illumination, depicted in Figure 3b. The characteristic PV parameters are reported in Table 1. All solar cells showed a high fill factor (FF, between 76 and 80% on average), indicating an efficient charge extraction of the photogenerated charge carriers. We also observed negligible hysteresis in between the forward and reverse scans, which suggests that either ion migration or interface recombination

https://doi.org/10.1021/acsenergylett.0c02445
ACS Energy Lett. 2021, 6, 827−836

(or both) are suppressed in these perovskite solar cells.[85,86] More interesting is the trend of the measured V_{oc}, which scales with the perovskite bandgap (Figure 3c), going from 1.14 V for the 1.70 eV absorber to 1.21 V for the largest 1.77 eV bandgap, on average. The corresponding V_{oc} deficit, defined as $(E_g/q - V_{oc})$, was found to be rather large (0.56−0.58 V) and constant through the series of devices, indicating a common origin of the nonradiative recombination channels. Although far from the radiative limit for these semiconductors (see discussion below), these values are the highest voltages obtained for wide-bandgap mixed-cation/halide perovskite solar cells deposited by vacuum deposition.

Overall, our wide-bandgap vacuum-deposited perovskite solar cells show PCEs of about 16% for bandgaps in the 1.70−1.75 eV range (Figure 3d). The best pixels were obtained for the wide-bandgap perovskite with E_g = 1.75 eV, with a PCE up to 16.8% (Figure S11). The reduction in efficiency observed for the solar cells with the highest bromide content are partially expected due to the increased bandgap (1.77 eV), although a small decrease in FF also contributes to the efficiency reduction.

In order to further assess the quality of the wide-bandgap $FA_{1-n}Cs_nPb(I_{1-x}Br_x)_3$ perovskites and the corresponding solar cells, we investigated their EQE response in the bandgap region. From the semilogarithmic plot in Figure 4a, one can see for all devices a steep drop of the EQE around the perovskite's bandgap.

From the slope, we extracted the Urbach energies (E_U, see Supporting Information for details), which are in the range of 16−18 meV, indicating a low electronic disorder that is essential to obtain high V_{oc}.[87] The bandgaps obtained from the derivative of the sensitive EQE measurements (Figure 4a) agree well with the values estimated from the Tauc plots in Figure 1b.[88] To be able to compare the limitations in the performance of absorbers with different bandgaps with each other, we divided the measured key performance indicators as obtained from the $J-V$ curves by their maximal obtainable values in Figure 4b. The radiative limit of the V_{oc} ($V_{oc,rad}$) was calculated via the EQE response,[89] while the FF and J_{sc} were obtained directly from detailed balance calculations given the specific bandgap of each material (SQ limit).[90,91] In general, all device parameters were found to be approximately at 80−90% of the theoretical maxima, highlighting the high quality of the perovskite films and devices reported here. The FF shows the highest ratio of the three parameters, indicating good rectification and low series resistance. We noted that the solar cells prepared with the 1.75 eV perovskite showed consistently higher FF, which might originate from a larger charge carrier mobility for this particular composition. The J_{sc} and V_{oc} more severely limit the overall performance, with ratios only slightly above 80%. Interestingly, the $V_{oc}/V_{oc,rad}$ ratio rises marginally with the bandgap, in contrast to the commonly observed behavior. This behavior might be related to the increased amount of PbI_2 in the wider-bandgap material as seen from XRD, which has been reported to passivate trap states in perovskite films.[92,93] However, the EQE of the electroluminescence (EQE_{EL}), estimated from the obtained photovoltage (Figure 4c, $EQE_{EL} = \exp(V_{oc} - V_{oc,rad})/kT)$), is in the 10^{-5} to 10^{-4} range for all devices, indicating the presence of nonradiative recombination either in the perovskite bulk or at the interface with the transport layers.[53−55] In order to shed light on the more relevant type of recombination, we evaluated the PL intensity of a perovskite film with and without the charge transport layers. As shown in Figure S13, the transport layers do quench the perovskite luminescence, indicating the presence of interface recombination. However, if we consider the relative PLQY obtained by integrating the PL spectra and normalizing it to the PL of the bare perovskite, we can estimate the QFLS difference in the presence of the transport materials. The difference in QFLS between the full stack (TaTm/perovskite/C_{60}) and a bare perovskite film is only about 50 mV. From this observation and taking into account that the V_{oc} of a device is about 300 mV lower compared to its radiative limit, we can conclude that the V_{oc} is mainly limited by nonradiative recombination in the bulk of the perovskite layer. Hence, future efforts should be directed toward passivation of bulk defects, through the use of additives or by modulating the deposition process. A possible loss pathway is the formation of iodide-rich domains driven by currents and electric fields, which would reduce the QFLS and hence the maximum attainable V_{oc}. It has been reported that even perovskite compositions that are stable under illumination can show halide segregation under current injection, which is evidenced by the EL spectrum of the diodes.[94] Hence, we tested our series of perovskite solar cells in forward bias, applying a current-density equivalent to their J_{sc}, and recorded the EL spectra as a function of time. Measurements are taken for up to 10 min as the EL intensity decreases over time (Figure S14) so that after 10−15 min, the spectrometer cannot resolve the spectra anymore due to the low signal-to-noise ratio. As highlighted in Figure 4d, the wide-bandgap solar cells were found to be very stable also under current injection, with the EL spectra showing a single component and no spectral changes over time. The EL spectral positions are also in agreement with the PL signals depicted in Figure 1d. Therefore, we exclude halide segregation as a main loss factor.

We finally evaluated the stability of the most efficient solar cells based on $FA_{1-n}Cs_nPb(I_{1-x}Br_x)_3$ perovskites with E_g = 1.75 eV. Both the shelf life (in the dark) and the operational stability under illumination were evaluated. The devices were encapsulated with a UV-curable resin and a glass slide, and the stability was evaluated in a nitrogen atmosphere to minimize the effect of environmental factors on the degradation (note that no differences in performance were observed after encapsulation, see Figure S15). For the shelf life stability, the $J-V$ characteristics under 1 sun illumination were recorded periodically at room temperature (Figure 5a).

After 500 h of storage (3 weeks), the PCE was found unvaried from the initial value, indicating an overall good stability of the perovskite film within the device structure used here. To evaluate the operational stability, the devices were maintained at their maximum power point (MPP) under a simulated 1 sun illumination with white LEDs at RT (25 °C) in nitrogen (Figure 5b). Under these operational conditions, the solar cell exhibited a remarkable stability, maintaining 90% of the initial PCE after 340 h (more than 2 weeks) of continuous operation.

In summary, we showed the room temperature preparation of wide-bandgap perovskite films of the type $FA_{1-n}Cs_nPb(I_{1-x}Br_x)_3$ by thermal vacuum deposition. The simultaneous sublimation of four precursors and in particular the use of $PbBr_2$ and CsI to individually control the bromide and cesium content allows the deposition of wide-bandgap perovskites with bandgaps between 1.7 and 1.8 eV. In this way, no signatures of halide segregation and an overall homogeneous morphology can be attained. These film properties translate

https://doi.org/10.1021/acsenergylett.0c02445
ACS Energy Lett. 2021, 6, 827−836

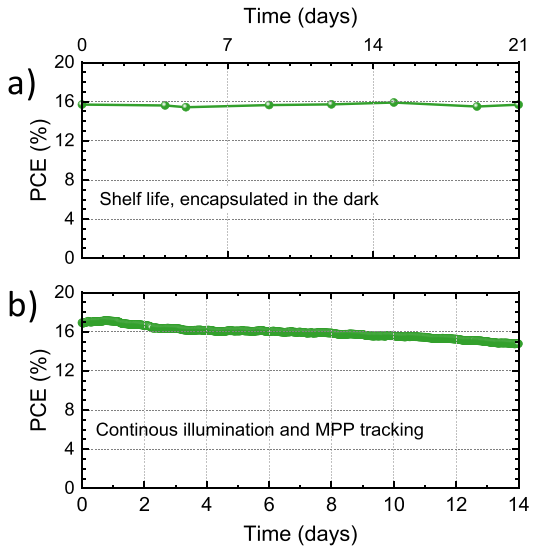

Figure 5. Stability assessment of wide-bandgap $FA_{0.65}Cs_{0.35}Pb(I_{0.73}Br_{0.27})_3$ perovskite solar cells with E_g = 1.75 eV, performed on encapsulated devices in a nitrogen atmosphere. (a) Shelf life measurements for devices kept in the dark. (b) Constant maximum power point tracking under continuous illumination.

into efficient p−i−n solar cells, with photovoltaic parameters at 80% of their maximum theoretical (radiative) limits, highlighting the high quality of the as-deposited perovskite semiconductors. We obtained solar cells with a bandgap of 1.75 eV and power conversion efficiency up to 16.8%. These devices retain 90% of their initial efficiency after more than 2 weeks of continuous operation. This work opens up the way toward the vacuum processing of photostable wide-bandgap perovskite solar cells for integration in tandem devices.

■ ASSOCIATED CONTENT

Supporting Information

The Supporting Information is available free of charge at https://pubs.acs.org/doi/10.1021/acsenergylett.0c02445.

Experimental methods, photoluminescence spectra analysis, XPS analysis, details of structural XRD analysis, device layout, details of calculation of bandgap, Urbach energy and radiative limit of the V_{oc} from EQE measurements, time-dependent electroluminescence intensity (PDF)

■ AUTHOR INFORMATION

Corresponding Author

Michele Sessolo − *Instituto de Ciencia Molecular, Universidad de Valencia, 46980 Paterna, Spain;* orcid.org/0000-0002-9189-3005; Email: michele.sessolo@uv.es

Authors

Lidón Gil-Escrig − *Instituto de Ciencia Molecular, Universidad de Valencia, 46980 Paterna, Spain*

Chris Dreessen − *Instituto de Ciencia Molecular, Universidad de Valencia, 46980 Paterna, Spain;* orcid.org/0000-0001-7444-6900

Francisco Palazon − *Instituto de Ciencia Molecular, Universidad de Valencia, 46980 Paterna, Spain;* orcid.org/0000-0002-1503-5965

Zafer Hawash − *Department of Physics, Karlstad University, SE-65188 Karlstad, Sweden;* orcid.org/0000-0001-9606-3521

Ellen Moons − *Department of Physics, Karlstad University, SE-65188 Karlstad, Sweden;* orcid.org/0000-0002-1609-8909

Steve Albrecht − *Young Investigator Group for Perovskite Tandem Solar Cells, Helmholtz-Center Berlin, 12489 Berlin, Germany;* orcid.org/0000-0001-9962-9535

Henk J. Bolink − *Instituto de Ciencia Molecular, Universidad de Valencia, 46980 Paterna, Spain;* orcid.org/0000-0001-9784-6253

Complete contact information is available at: https://pubs.acs.org/10.1021/acsenergylett.0c02445

Notes

The authors declare no competing financial interest.

■ ACKNOWLEDGMENTS

The research leading to these results has received funding from the European Union's Horizon 2020 research and innovation programme under grant agreement No. 763977 of the PERTPV project, the Spanish Ministry of Science, Innovation and Universities (MICIU, RTI2018-095362-A-I00, PCI2019-111829-2, and EQC2018-004888-P), and the Comunitat Valenciana (IDIFEDER/2018/061 and Prometeu/2020/077). C.D. acknowledges that the project that gave rise to these results received the support of a fellowship from "la Caixa" Foundation (ID 100010434, code LCF/BQ/DI19/11730020). M.S. and F.P. acknowledge the MICIU for their RyC and JdC contracts, respectively. S.A. acknowledges funding from the Federal Ministry of Education and Research (BMBF) for funding of the Young Investigator Group for Perovskite Tandem Solar Cells within the program "Materialforschung für die Energiewende" (grant no. 03SF0540), the Helmholtz Association within the HySPRINT Innovation lab project, and the HyPerCells Joint Graduate School. Z.H. and E.M. acknowledge SOLAR-ERA.NET and the Swedish Energy Council (Energimyndigheten, contract 48381-1) for the PERDRY project.

■ REFERENCES

(1) Snaith, H. J.; Hacke, P. Enabling Reliability Assessments of Pre-Commercial Perovskite Photovoltaics with Lessons Learned from Industrial Standards. *Nat. Energy* **2018**, *3* (6), 459−465.

(2) Li, Z.; Klein, T. R.; Kim, D. H.; Yang, M.; Berry, J. J.; van Hest, M. F. A. M.; Zhu, K. Scalable Fabrication of Perovskite Solar Cells. *Nat. Rev. Mater.* **2018**, *3* (4), 18017.

(3) Park, N.-G.; Grätzel, M.; Miyasaka, T.; Zhu, K.; Emery, K. Towards Stable and Commercially Available Perovskite Solar Cells. *Nat. Energy* **2016**, *1* (11), 16152.

(4) Dunlap-Shohl, W. A.; Zhou, Y.; Padture, N. P.; Mitzi, D. B. Synthetic Approaches for Halide Perovskite Thin Films. *Chem. Rev.* **2019**, *119* (5), 3193−3295.

(5) Swartwout, R.; Hoerantner, M. T.; Bulović, V. Scalable Deposition Methods for Large-area Production of Perovskite Thin Films. *Energy Environ. Mater.* **2019**, *2* (2), 119−145.

(6) Park, N.-G.; Zhu, K. Scalable Fabrication and Coating Methods for Perovskite Solar Cells and Solar Modules. *Nat. Rev. Mater.* **2020**, *5* (5), 333−350.

(7) Yin, W.-J.; Shi, T.; Yan, Y. Unique Properties of Halide Perovskites as Possible Origins of the Superior Solar Cell Performance. *Adv. Mater.* **2014**, *26* (27), 4653−4658.

(8) Chu, W.; Zheng, Q.; Prezhdo, O. V.; Zhao, J.; Saidi, W. A. Low-Frequency Lattice Phonons in Halide Perovskites Explain High Defect Tolerance toward Electron-Hole Recombination. *Sci. Adv.* **2020**, *6* (7), No. eaaw7453.
(9) De Wolf, S.; Holovsky, J.; Moon, S.-J.; Löper, P.; Niesen, B.; Ledinsky, M.; Haug, F.-J.; Yum, J.-H.; Ballif, C. Organometallic Halide Perovskites: Sharp Optical Absorption Edge and Its Relation to Photovoltaic Performance. *J. Phys. Chem. Lett.* **2014**, *5* (6), 1035−1039.
(10) Adinolfi, V.; Yuan, M.; Comin, R.; Thibau, E. S.; Shi, D.; Saidaminov, M. I.; Kanjanaboos, P.; Kopilovic, D.; Hoogland, S.; Lu, Z.-H.; et al. The In-Gap Electronic State Spectrum of Methylammonium Lead Iodide Single-Crystal Perovskites. *Adv. Mater.* **2016**, *28* (17), 3406−3410.
(11) Stranks, S. D.; Eperon, G. E.; Grancini, G.; Menelaou, C.; Alcocer, M. J. P.; Leijtens, T.; Herz, L. M.; Petrozza, A.; Snaith, H. J. Electron-Hole Diffusion Lengths Exceeding 1 Micrometer in an Organometal Trihalide Perovskite Absorber. *Science (Washington, DC, U. S.)* **2013**, *342* (6156), 341−344.
(12) Brenner, T. M.; Egger, D. A.; Kronik, L.; Hodes, G.; Cahen, D. Hybrid Organic—Inorganic Perovskites: Low-Cost Semiconductors with Intriguing Charge-Transport Properties. *Nat. Rev. Mater.* **2016**, *1* (1), 15007.
(13) Huang, J.; Yuan, Y.; Shao, Y.; Yan, Y. Understanding the Physical Properties of Hybrid Perovskites for Photovoltaic Applications. *Nat. Rev. Mater.* **2017**, *2* (7), 17042.
(14) Ball, J. M.; Petrozza, A. Defects in Perovskite-Halides and Their Effects in Solar Cells. *Nat. Energy* **2016**, *1* (11), 16149.
(15) Kojima, A.; Teshima, K.; Shirai, Y.; Miyasaka, T. Organometal Halide Perovskites as Visible-Light Sensitizers for Photovoltaic Cells. *J. Am. Chem. Soc.* **2009**, *131* (17), 6050−6051.
(16) Green, M. A.; Dunlop, E. D.; Hohl-Ebinger, J.; Yoshita, M.; Kopidakis, N.; Ho-Baillie, A. W. Y. Solar Cell Efficiency Tables (Version 55). *Prog. Photovoltaics* **2020**, *28* (1), 3−15.
(17) Noh, J. H.; Im, S. H.; Heo, J. H.; Mandal, T. N.; Seok, S. Il Chemical Management for Colorful, Efficient, and Stable Inorganic-Organic Hybrid Nanostructured Solar Cells. *Nano Lett.* **2013**, *13* (4), 1764−1769.
(18) Eperon, G. E.; Stranks, S. D.; Menelaou, C.; Johnston, M. B.; Herz, L. M.; Snaith, H. J. Formamidinium Lead Trihalide: A Broadly Tunable Perovskite for Efficient Planar Heterojunction Solar Cells. *Energy Environ. Sci.* **2014**, *7* (3), 982.
(19) Protesescu, L.; Yakunin, S.; Bodnarchuk, M. I.; Krieg, F.; Caputo, R.; Hendon, C. H.; Yang, R. X.; Walsh, A.; Kovalenko, M. V. Nanocrystals of Cesium Lead Halide Perovskites (CsPbX 3, X = Cl, Br, and I): Novel Optoelectronic Materials Showing Bright Emission with Wide Color Gamut. *Nano Lett.* **2015**, *15* (6), 3692−3696.
(20) Sutton, R. J.; Eperon, G. E.; Miranda, L.; Parrott, E. S.; Kamino, B. A.; Patel, J. B.; Hörantner, M. T.; Johnston, M. B.; Haghighirad, A. A.; Moore, D. T.; et al. Bandgap-Tunable Cesium Lead Halide Perovskites with High Thermal Stability for Efficient Solar Cells. *Adv. Energy Mater.* **2016**, *6* (8), 1502458.
(21) Eperon, G. E.; Hörantner, M. T.; Snaith, H. J. Metal Halide Perovskite Tandem and Multiple-Junction Photovoltaics. *Nat. Rev. Chem.* **2017**, *1* (12), 0095.
(22) Leijtens, T.; Bush, K. A.; Prasanna, R.; McGehee, M. D. Opportunities and Challenges for Tandem Solar Cells Using Metal Halide Perovskite Semiconductors. *Nat. Energy* **2018**, *3* (10), 828−838.
(23) Jošt, M.; Kegelmann, L.; Korte, L.; Albrecht, S. Monolithic Perovskite Tandem Solar Cells: A Review of the Present Status and Advanced Characterization Methods Toward 30% Efficiency. *Adv. Energy Mater.* **2020**, *10* (26), 1904102.
(24) Wang, Z.; Song, Z.; Yan, Y.; Liu, S.; Yang, D. Perovskite—a Perfect Top Cell for Tandem Devices to Break the S-Q Limit. *Adv. Sci.* **2019**, *6* (7), 1801704.
(25) Han, Q.; Hsieh, Y.-T.; Meng, L.; Wu, J.-L.; Sun, P.; Yao, E.-P.; Chang, S.-Y.; Bae, S.-H.; Kato, T.; Bermudez, V.; et al. High-Performance Perovskite/Cu(In,Ga)Se 2 Monolithic Tandem Solar Cells. *Science (Washington, DC, U. S.)* **2018**, *361* (6405), 904−908.
(26) Al-Ashouri, A.; Magomedov, A.; Roß, M.; Jošt, M.; Talaikis, M.; Chistiakova, G.; Bertram, T.; Márquez, J. A.; Köhnen, E.; Kasparavičius, E.; et al. Conformal Monolayer Contacts with Lossless Interfaces for Perovskite Single Junction and Monolithic Tandem Solar Cells. *Energy Environ. Sci.* **2019**, *12* (11), 3356−3369.
(27) Kim, D. H.; Muzzillo, C. P.; Tong, J.; Palmstrom, A. F.; Larson, B. W.; Choi, C.; Harvey, S. P.; Glynn, S.; Whitaker, J. B.; Zhang, F.; et al. Bimolecular Additives Improve Wide-Band-Gap Perovskites for Efficient Tandem Solar Cells with CIGS. *Joule* **2019**, *3* (7), 1734−1745.
(28) Lang, F.; Jošt, M.; Frohna, K.; Köhnen, E.; Al-Ashouri, A.; Bowman, A. R.; Bertram, T.; Morales-Vilches, A. B.; Koushik, D.; Tennyson, E. M.; et al. Proton Radiation Hardness of Perovskite Tandem Photovoltaics. *Joule* **2020**, *4* (5), 1054−1069.
(29) Jošt, M.; Köhnen, E.; Morales-Vilches, A. B.; Lipovšek, B.; Jäger, K.; Macco, B.; Al-Ashouri, A.; Krč, J.; Korte, L.; Rech, B.; et al. Textured Interfaces in Monolithic Perovskite/Silicon Tandem Solar Cells: Advanced Light Management for Improved Efficiency and Energy Yield. *Energy Environ. Sci.* **2018**, *11*, 3511−3523.
(30) Sahli, F.; Werner, J.; Kamino, B. A.; Bräuninger, M.; Monnard, R.; Paviet-Salomon, B.; Barraud, L.; Ding, L.; Diaz Leon, J. J.; Sacchetto, D.; et al. Fully Textured Monolithic Perovskite/Silicon Tandem Solar Cells with 25.2% Power Conversion Efficiency. *Nat. Mater.* **2018**, *17* (9), 820−826.
(31) Kim, D.; Jung, H. J.; Park, I. J.; Larson, B. W.; Dunfield, S. P.; Xiao, C.; Kim, J.; Tong, J.; Boonmongkolras, P.; Ji, S. G.; et al. Efficient, Stable Silicon Tandem Cells Enabled by Anion-Engineered Wide-Bandgap Perovskites. *Science (Washington, DC, U. S.)* **2020**, *368* (6487), 155−160.
(32) Chen, B.; Baek, S.-W.; Hou, Y.; Aydin, E.; De Bastiani, M.; Scheffel, B.; Proppe, A.; Huang, Z.; Wei, M.; Wang, Y.-K.; et al. Enhanced Optical Path and Electron Diffusion Length Enable High-Efficiency Perovskite Tandems. *Nat. Commun.* **2020**, *11* (1), 1257.
(33) Xu, J.; Boyd, C. C.; Yu, Z. J.; Palmstrom, A. F.; Witter, D. J.; Larson, B. W.; France, R. M.; Werner, J.; Harvey, S. P.; Wolf, E. J.; et al. Triple-Halide Wide-Band Gap Perovskites with Suppressed Phase Segregation for Efficient Tandems. *Science (Washington, DC, U. S.)* **2020**, *367* (6482), 1097−1104.
(34) Hou, Y.; Aydin, E.; De Bastiani, M.; Xiao, C.; Isikgor, F. H.; Xue, D.-J.; Chen, B.; Chen, H.; Bahrami, B.; Chowdhury, A. H.; et al. Efficient Tandem Solar Cells with Solution-Processed Perovskite on Textured Crystalline Silicon. *Science (Washington, DC, U. S.)* **2020**, *367* (6482), 1135−1140.
(35) Coletti, G.; Luxembourg, S. L.; Geerligs, L. J.; Rosca, V.; Burgers, A. R.; Wu, Y.; Okel, L.; Kloos, M.; Danzl, F. J. K.; Najafi, M.; et al. Bifacial Four-Terminal Perovskite/Silicon Tandem Solar Cells and Modules. *ACS Energy Lett.* **2020**, *5* (5), 1676−1680.
(36) Eperon, G. E.; Leijtens, T.; Bush, K. A.; Prasanna, R.; Green, T.; Wang, J. T.-W.; McMeekin, D. P.; Volonakis, G.; Milot, R. L.; May, R.; et al. Perovskite-Perovskite Tandem Photovoltaics with Optimized Band Gaps. *Science (Washington, DC, U. S.)* **2016**, *354* (6314), 861−865.
(37) Forgács, D.; Gil-Escrig, L.; Pérez-Del-Rey, D.; Momblona, C.; Werner, J.; Niesen, B.; Ballif, C.; Sessolo, M.; Bolink, H. J. Efficient Monolithic Perovskite/Perovskite Tandem Solar Cells. *Adv. Energy Mater.* **2017**, *7* (8), 1602121.
(38) Zhao, D.; Chen, C.; Wang, C.; Junda, M. M.; Song, Z.; Grice, C. R.; Yu, Y.; Li, C.; Subedi, B.; Podraza, N. J.; et al. Efficient Two-Terminal All-Perovskite Tandem Solar Cells Enabled by High-Quality Low-Bandgap Absorber Layers. *Nat. Energy* **2018**, *3* (12), 1093−1100.
(39) Palmstrom, A. F.; Eperon, G. E.; Leijtens, T.; Prasanna, R.; Habisreutinger, S. N.; Nemeth, W.; Gaulding, E. A.; Dunfield, S. P.; Reese, M.; Nanayakkara, S.; et al. Enabling Flexible All-Perovskite Tandem Solar Cells. *Joule* **2019**, *3* (9), 2193−2204.
(40) Yang, Z.; Yu, Z.; Wei, H.; Xiao, X.; Ni, Z.; Chen, B.; Deng, Y.; Habisreutinger, S. N.; Chen, X.; Wang, K.; et al. Enhancing Electron

https://doi.org/10.1021/acsenergylett.0c02445
ACS Energy Lett. 2021, 6, 827−836

Diffusion Length in Narrow-Bandgap Perovskites for Efficient Monolithic Perovskite Tandem Solar Cells. *Nat. Commun.* **2019**, *10* (1), 1−9.
(41) Lin, R.; Xiao, K.; Qin, Z.; Han, Q.; Zhang, C.; Wei, M.; Saidaminov, M. I.; Gao, Y.; Xu, J.; Xiao, M.; et al. Monolithic All-Perovskite Tandem Solar Cells with 24.8% Efficiency Exploiting Comproportionation to Suppress Sn(Ii) Oxidation in Precursor Ink. *Nat. Energy* **2019**, *4* (10), 864−873.
(42) Tong, J.; Song, Z.; Kim, D. H.; Chen, X.; Chen, C.; Palmstrom, A. F.; Ndione, P. F.; Reese, M. O.; Dunfield, S. P.; Reid, O. G.; et al. Carrier Lifetimes of > 1 Ms in Sn-Pb Perovskites Enable Efficient All-Perovskite Tandem Solar Cells. *Science (Washington, DC, U. S.)* **2019**, *364* (6439), 475−479.
(43) Hao, F.; Stoumpos, C. C.; Chang, R. P. H.; Kanatzidis, M. G. Anomalous Band Gap Behavior in Mixed Sn and Pb Perovskites Enables Broadening of Absorption Spectrum in Solar Cells. *J. Am. Chem. Soc.* **2014**, *136* (22), 8094−8099.
(44) Prasanna, R.; Gold-Parker, A.; Leijtens, T.; Conings, B.; Babayigit, A.; Boyen, H.-G.; Toney, M. F.; McGehee, M. D. Band Gap Tuning via Lattice Contraction and Octahedral Tilting in Perovskite Materials for Photovoltaics. *J. Am. Chem. Soc.* **2017**, *139* (32), 11117−11124.
(45) Hoke, E. T.; Slotcavage, D. J.; Dohner, E. R.; Bowring, A. R.; Karunadasa, H. I.; McGehee, M. D. Reversible Photo-Induced Trap Formation in Mixed-Halide Hybrid Perovskites for Photovoltaics. *Chem. Sci.* **2015**, *6* (1), 613−617.
(46) McMeekin, D. P.; Sadoughi, G.; Rehman, W.; Eperon, G. E.; Saliba, M.; Horantner, M. T.; Haghighirad, A.; Sakai, N.; Korte, L.; Rech, B.; et al. A Mixed-Cation Lead Mixed-Halide Perovskite Absorber for Tandem Solar Cells. *Science (Washington, DC, U. S.)* **2016**, *351* (6269), 151−155.
(47) Bush, K. A.; Frohna, K.; Prasanna, R.; Beal, R. E.; Leijtens, T.; Swifter, S. A.; McGehee, M. D. Compositional Engineering for Efficient Wide Band Gap Perovskites with Improved Stability to Photoinduced Phase Segregation. *ACS Energy Lett.* **2018**, *3* (2), 428−435.
(48) Yang, T. C.-J.; Fiala, P.; Jeangros, Q.; Ballif, C. High-Bandgap Perovskite Materials for Multijunction Solar Cells. *Joule* **2018**, *2* (8), 1421−1436.
(49) Gharibzadeh, S.; Abdollahi Nejand, B.; Jakoby, M.; Abzieher, T.; Hauschild, D.; Moghadamzadeh, S.; Schwenzer, J. A.; Brenner, P.; Schmager, R.; Haghighirad, A. A.; et al. Record Open-Circuit Voltage Wide-Bandgap Perovskite Solar Cells Utilizing 2D/3D Perovskite Heterostructure. *Adv. Energy Mater.* **2019**, *9* (21), 1803699.
(50) Rajagopal, A.; Stoddard, R. J.; Jo, S. B.; Hillhouse, H. W.; Jen, A. K. Y. Overcoming the Photovoltage Plateau in Large Bandgap Perovskite Photovoltaics. *Nano Lett.* **2018**, *18* (6), 3985−3993.
(51) Peña-Camargo, F.; Caprioglio, P.; Zu, F.; Gutierrez-Partida, E.; Wolff, C. M.; Brinkmann, K.; Albrecht, S.; Riedl, T.; Koch, N.; Neher, D.; et al. Halide Segregation versus Interfacial Recombination in Bromide-Rich Wide-Gap Perovskite Solar Cells. *ACS Energy Lett.* **2020**, *5* (8), 2728−2736.
(52) Liu, Z.; Krückemeier, L.; Krogmeier, B.; Klingebiel, B.; Márquez, J. A.; Levcenko, S.; Öz, S.; Mathur, S.; Rau, U.; Unold, T.; et al. Open-Circuit Voltages Exceeding 1.26 V in Planar Methylammonium Lead Iodide Perovskite Solar Cells. *ACS Energy Lett.* **2019**, *4* (1), 110−117.
(53) Wolff, C. M.; Caprioglio, P.; Stolterfoht, M.; Neher, D. Nonradiative Recombination in Perovskite Solar Cells: The Role of Interfaces. *Adv. Mater.* **2019**, *31* (52), 1902762.
(54) deQuilettes, D. W.; Frohna, K.; Emin, D.; Kirchartz, T.; Bulovic, V.; Ginger, D. S.; Stranks, S. D. Charge-Carrier Recombination in Halide Perovskites. *Chem. Rev.* **2019**, *119* (20), 11007−11019.
(55) Mahesh, S.; Ball, J. M.; Oliver, R. D. J.; McMeekin, D. P.; Nayak, P. K.; Johnston, M. B.; Snaith, H. J. Revealing the Origin of Voltage Loss in Mixed-Halide Perovskite Solar Cells. *Energy Environ. Sci.* **2020**, *13* (1), 258−267.
(56) Aydin, E.; Bastiani, M.; Wolf, S. Defect and Contact Passivation for Perovskite Solar Cells. *Adv. Mater.* **2019**, *31* (25), 1900428.
(57) Kim, J.; Ho-Baillie, A.; Huang, S. Review of Novel Passivation Techniques for Efficient and Stable Perovskite Solar Cells. *Sol. RRL* **2019**, *3* (4), 1800302.
(58) Gao, F.; Zhao, Y.; Zhang, X.; You, J. Recent Progresses on Defect Passivation toward Efficient Perovskite Solar Cells. *Adv. Energy Mater.* **2020**, *10* (13), 1902650.
(59) Akin, S.; Arora, N.; Zakeeruddin, S. M.; Grätzel, M.; Friend, R. H.; Dar, M. I. New Strategies for Defect Passivation in High-Efficiency Perovskite Solar Cells. *Adv. Energy Mater.* **2020**, *10* (13), 1903090.
(60) Chen, B.; Rudd, P. N.; Yang, S.; Yuan, Y.; Huang, J. Imperfections and Their Passivation in Halide Perovskite Solar Cells. *Chem. Soc. Rev.* **2019**, *48* (14), 3842−3867.
(61) Lin, Q.; Armin, A.; Nagiri, R. C. R.; Burn, P. L.; Meredith, P. Electro-Optics of Perovskite Solar Cells. *Nat. Photonics* **2015**, *9* (2), 106−112.
(62) Hsiao, S.-Y.; Lin, H.-L.; Lee, W.-H.; Tsai, W.-L.; Chiang, K.-M.; Liao, W.-Y.; Ren-Wu, C.-Z.; Chen, C.-Y.; Lin, H.-W. Efficient All-Vacuum Deposited Perovskite Solar Cells by Controlling Reagent Partial Pressure in High Vacuum. *Adv. Mater.* **2016**, *28* (32), 7013−7019.
(63) Li, J.; Wang, H.; Chin, X. Y.; Dewi, H. A.; Vergeer, K.; Goh, T. W.; Lim, J. W. M.; Lew, J. H.; Loh, K. P.; Soci, C.; et al. Highly Efficient Thermally Co-Evaporated Perovskite Solar Cells and Mini-Modules. *Joule* **2020**, *4* (5), 1035−1053.
(64) Ávila, J.; Momblona, C.; Boix, P.; Sessolo, M.; Anaya, M.; Lozano, G.; Vandewal, K.; Míguez, H.; Bolink, H. J. High Voltage Vacuum-Deposited CH 3 NH 3 PbI 3 -CH 3 NH 3 PbI 3 Tandem Solar Cells. *Energy Environ. Sci.* **2018**, *11* (11), 3292−3297.
(65) Liu, M.; Johnston, M. B.; Snaith, H. J. Efficient Planar Heterojunction Perovskite Solar Cells by Vapour Deposition. *Nature* **2013**, *501* (7467), 395−398.
(66) Malinkiewicz, O.; Yella, A.; Lee, Y. H.; Espallargas, G. M.; Graetzel, M.; Nazeeruddin, M. K.; Bolink, H. J. Perovskite Solar Cells Employing Organic Charge-Transport Layers. *Nat. Photonics* **2014**, *8* (2), 128−132.
(67) Momblona, C.; Gil-Escrig, L.; Bandiello, E.; Hutter, E. M.; Sessolo, M.; Lederer, K.; Blochwitz-Nimoth, J.; Bolink, H. J. Efficient Vacuum Deposited P-i-n and n-i-p Perovskite Solar Cells Employing Doped Charge Transport Layers. *Energy Environ. Sci.* **2016**, *9* (11), 3456−3463.
(68) Al-Ashouri, A.; Magomedov, A.; Roß, M.; Jošt, M.; Talaikis, M.; Chistiakova, G.; Bertram, T.; Márquez, J. A.; Köhnen, E.; Kasparavičius, E.; et al. Conformal Monolayer Contacts with Lossless Interfaces for Perovskite Single Junction and Monolithic Tandem Solar Cells. *Energy Environ. Sci.* **2019**, *12* (11), 3356−3369.
(69) Longo, G.; Momblona, C.; La-Placa, M.-G.; Gil-Escrig, L.; Sessolo, M.; Bolink, H. J. Fully Vacuum-Processed Wide Band Gap Mixed-Halide Perovskite Solar Cells. *ACS Energy Lett.* **2018**, *3* (1), 214−219.
(70) Slotcavage, D. J.; Karunadasa, H. I.; McGehee, M. D. Light-Induced Phase Segregation in Halide-Perovskite Absorbers. *ACS Energy Lett.* **2016**, *1* (6), 1199−1205.
(71) Knight, A. J.; Herz, L. M. Preventing Phase Segregation in Mixed-Halide Perovskites: A Perspective. *Energy Environ. Sci.* **2020**, *13* (7), 2024−2046.
(72) Huang, J.; Xiang, S.; Yu, J.; Li, C.-Z. Highly Efficient Prismatic Perovskite Solar Cells. *Energy Environ. Sci.* **2019**, *12* (3), 929−937.
(73) Gil-Escrig, L.; Momblona, C.; La-Placa, M.-G.; Boix, P. P.; Sessolo, M.; Bolink, H. J. Vacuum Deposited Triple-Cation Mixed-Halide Perovskite Solar Cells. *Adv. Energy Mater.* **2018**, *8* (14), 1703506.
(74) Ji, R.; Zhang, Z.; Cho, C.; An, Q.; Paulus, F.; Kroll, M.; Löffler, M.; Nehm, F.; Rellinghaus, B.; Leo, K.; et al. Thermally Evaporated Methylammonium-Free Perovskite Solar Cells. *J. Mater. Chem. C* **2020**, *8* (23), 7725−7733.

https://doi.org/10.1021/acsenergylett.0c02445
ACS Energy Lett. 2021, 6, 827−836

(75) Chiang, Y.; Anaya, M.; Stranks, S. D. Multisource Vacuum Deposition of Methylammonium-Free Perovskite Solar Cells. *ACS Energy Lett.* **2020**, *5* (8), 2498−2504.
(76) Kim, B.-S.; Gil-Escrig, L.; Sessolo, M.; Bolink, H. J. Deposition Kinetics and Compositional Control of Vacuum-Processed CH 3 NH 3 PbI 3 Perovskite. *J. Phys. Chem. Lett.* **2020**, *11* (16), 6852−6859.
(77) Gil-Escrig, L.; Dreessen, C.; Kaya, I. C.; Kim, B.-S.; Palazon, F.; Sessolo, M.; Bolink, H. J. Efficient Vacuum-Deposited Perovskite Solar Cells with Stable Cubic FA 1- x MA x PbI 3. *ACS Energy Lett.* **2020**, *5*, 3053−3061.
(78) Scofield, J. H. Hartree-Slater Subshell Photoionization Cross-Sections at 1254 and 1487 EV. *J. Electron Spectrosc. Relat. Phenom.* **1976**, *8* (2), 129−137.
(79) Seah, M. P.; Dench, W. A. Quantitative Electron Spectroscopy of Surfaces: A Standard Data Base for Electron Inelastic Mean Free Paths in Solids. *Surf. Interface Anal.* **1979**, *1* (1), 2−11.
(80) Goldstein, J. I.; Newbury, D. E.; Michael, J. R.; Ritchie, N. W. M.; Scott, J. H. J.; Joy, D. C. Qualitative Elemental Analysis by Energy Dispersive X-Ray Spectrometry. *Scanning Electron Microscopy and X-Ray Microanalysis* **2018**, 265−287.
(81) Akkerman, Q. A.; Manna, L. What Defines a Halide Perovskite? *ACS Energy Lett.* **2020**, *5*, 604−610.
(82) Momblona, C.; Gil-Escrig, L.; Bandiello, E.; Hutter, E. M.; Sessolo, M.; Lederer, K.; Blochwitz-Nimoth, J.; Bolink, H. J. Efficient Vacuum Deposited P-i-n and n-i-p Perovskite Solar Cells Employing Doped Charge Transport Layers. *Energy Environ. Sci.* **2016**, *9* (11), 3456−3463.
(83) Roß, M.; Gil-Escrig, L.; Al-Ashouri, A.; Tockhorn, P.; Jošt, M.; Rech, B.; Albrecht, S. Co-Evaporated p-i-n Perovskite Solar Cells beyond 20% Efficiency: Impact of Substrate Temperature and Hole-Transport Layer. *ACS Appl. Mater. Interfaces* **2020**, *12* (35), 39261−39272.
(84) Lohmann, K. B.; Patel, J. B.; Rothmann, M. U.; Xia, C. Q.; Oliver, R. D. J.; Herz, L. M.; Snaith, H. J.; Johnston, M. B. Control over Crystal Size in Vapor Deposited Metal-Halide Perovskite Films. *ACS Energy Lett.* **2020**, *5* (3), 710−717.
(85) van Reenen, S.; Kemerink, M.; Snaith, H. J. Modeling Anomalous Hysteresis in Perovskite Solar Cells. *J. Phys. Chem. Lett.* **2015**, *6* (19), 3808−3814.
(86) Calado, P.; Telford, A. M.; Bryant, D.; Li, X.; Nelson, J.; O'Regan, B. C.; Barnes, P. R. F. Evidence for Ion Migration in Hybrid Perovskite Solar Cells with Minimal Hysteresis. *Nat. Commun.* **2016**, *7* (1), 13831.
(87) Chantana, J.; Kawano, Y.; Nishimura, T.; Mavlonov, A.; Minemoto, T. Impact of Urbach Energy on Open-Circuit Voltage Deficit of Thin-Film Solar Cells. *Sol. Energy Mater. Sol. Cells* **2020**, *210*, 110502.
(88) Rau, U.; Blank, B.; Müller, T. C. M.; Kirchartz, T. Efficiency Potential of Photovoltaic Materials and Devices Unveiled by Detailed-Balance Analysis. *Phys. Rev. Appl.* **2017**, *7* (4), 44016.
(89) Rau, U. Reciprocity Relation between Photovoltaic Quantum Efficiency and Electroluminescent Emission of Solar Cells. *Phys. Rev. B: Condens. Matter Mater. Phys.* **2007**, *76* (8), 85303.
(90) Shockley, W.; Queisser, H. J. Detailed Balance Limit of Efficiency of P-n Junction Solar Cells. *J. Appl. Phys.* **1961**, *32* (3), 510−519.
(91) Rühle, S. Tabulated Values of the Shockley-Queisser Limit for Single Junction Solar Cells. *Sol. Energy* **2016**, *130*, 139−147.
(92) Chen, Q.; Zhou, H.; Song, T.-B.; Luo, S.; Hong, Z.; Duan, H.-S.; Dou, L.; Liu, Y.; Yang, Y. Controllable Self-Induced Passivation of Hybrid Lead Iodide Perovskites toward High Performance Solar Cells. *Nano Lett.* **2014**, *14* (7), 4158−4163.
(93) Lee, J.-W.; Kim, S.-G.; Bae, S.-H.; Lee, D.-K.; Lin, O.; Yang, Y.; Park, N.-G. The Interplay between Trap Density and Hysteresis in Planar Heterojunction Perovskite Solar Cells. *Nano Lett.* **2017**, *17* (7), 4270−4276.
(94) Braly, I. L.; Stoddard, R. J.; Rajagopal, A.; Uhl, A. R.; Katahara, J. K.; Jen, A. K. Y.; Hillhouse, H. W. Current-Induced Phase Segregation in Mixed Halide Hybrid Perovskites and Its Impact on Two-Terminal Tandem Solar Cell Design. *ACS Energy Lett.* **2017**, *2* (8), 1841−1847.

NOTE ADDED AFTER ISSUE PUBLICATION

This article was initially published with an incorrect copyright statement and was corrected on or around May 5, 2021.

https://doi.org/10.1021/acsenergylett.0c02445
ACS Energy Lett. 2021, 6, 827−836